Characteristic analysis of a slotless self-bearing motor

Huy Kiet Ngo[1], Trung Tuyen Bui[1,2], Anh Quan Pham Doan[1], Thao Nhi Nguyen[1], Quang Dang Pham[1], Van Nam Giap[1], Dang Quang Bui[1], Quang Dich Nguyen[1*]

[1]Hanoi University of Science and Technology
[2]Vinh University of Technology Education
[*]Corresponding author E-mail: dich.nguyenquang@hust.edu.vn
DOI: https://doi.org/10.64032/mca.v30i2.394

Abstract

This paper presents a comprehensive experimental validation of a 3-DOF SSBM prototype, focusing on the characterization of radial bearing forces (F_x, F_y) and rotational torque (τ). The study verifies the theoretical Lorentz force model through static loading and dynamic speed tests. The results demonstrate a high degree of linearity in forces and torque generation, with average relative errors of approximately 0.87%, 3.51% for the radial forces F_x and F_y, respectively, and 0.97% for rotational torque. Furthermore, the decoupling capability of the winding configuration is confirmed, as the generated radial forces exhibit independence from the rotor phase angle. However, dynamic tests reveal that rotational speed significantly influences the force-current relationship; while the model remains accurate at low speeds, coupling effects cause a deviation of up to 16.9% at 2,500 rpm. These findings define the operational limits of the linear model and highlight the necessity for speed-dependent compensation in future research.

Symbols

Symbols	Units	Description
τ	N·m	Motor torque
f_x	N	x-axis bearing force
f_y	N	y-axis bearing force
i_m	A	Torque current
i_x	A	Bearing force f_x current
i_y	A	Bearing force f_y current
$k_{nm}\ k_m$		Torque coefficient
$k_{nb}\ k_b$		Bearing force coefficient
l_p	m	Length of parallel segment of 1 winding
l_t	m	Length of serial segment of 1 winding
r	m	Rotor radius
B_0	T	Maximum magnetic flux density in the air gap
α	rad	Rotor angular position
β	rad	Torque current phase angle

Abbreviations

SBM	Self-bearing motor
SSBM	Slotless self-bearing motor
rpm	round(s) per minute
2D	two-dimensional

1. Introduction

Self-bearing motors (SBMs) represent a distinctive class of electric machines that have garnered increasing research attention in recent years due to their unique structural and functional characteristics. Unlike conventional motors, which rely on mechanical ball bearings and are limited to generating rotational torque, SBMs are capable of simultaneously producing torque and bearing forces on the rotor. This dual functionality facilitates the integration of rotor position control and rotational motion within a unified configuration. By eliminating the need for traditional bearings, SBMs reduce friction, enhance wear resistance, and minimize lubrication requirements. These advantages make SBMs particularly suitable for high-speed and ultra-high-speed applications [1–3].

A prominent subclass of SBMs is the slotless self-bearing motor (SSBM). Building upon earlier investigations into permanent-magnet-based SBMs, research on SSBMs began to emerge in the early 2000s [4–5]. A defining structural feature of SSBMs is the absence of stator teeth, which effectively mitigates cogging torque and contributes to smoother operation. This design, combined with inherent self-bearing capabilities, renders SSBMs highly suitable for applications requiring low vibration and high rotational speeds. Foundational studies [4–5] introduced the basic architecture of SSBMs, formulated theoretical models to describe their operating principles, and experimentally verified their self-bearing and torque-generation capabilities.

In 2006, a methodology based on the Maxwell stress tensor was employed to derive force and torque-current relationships for large-scale motors, thereby simplifying controller design and highlighting the linear dependence between electromagnetic force/torque and their respective currents [6–7]. The high-speed potential of SSBMs was first emphasized in 2009, although practical implementations at the time were limited to approximately 5,000 revolutions per minute (rpm) [8]. Substantial progress in high-speed operation was achieved throughout the 2010s [9–10]. Notably, a prototype developed in 2014 attained rotational speeds of up to 500,000 rpm. That study also demonstrated the feasibility of SSBM operation in vacuum environments

through comprehensive electromagnetic and mechanical modeling.

Recent research efforts have increasingly focused on optimizing motor design and control strategies. For example, improvements in force and torque coefficients have been achieved through enhancements in winding configurations and electromagnetic circuit design, leading to increased motor efficiency. Concurrently, advanced control algorithms have been developed to improve dynamic response and system stability [12–13].

Despite these advancements, the majority of existing studies have primarily concentrated on theoretical formulations and finite element analysis (FEA) simulations. While some experimental validations have been reported, they often focus solely on demonstrating basic self-bearing and rotational functionalities or controller performance, without providing detailed characterization of motor parameters. To address this gap, the present study aims to experimentally investigate key motor characteristics.

This work utilizes an SSBM configuration featuring three degrees of freedom (3-DOF) control, including rotation about the z-axis and translational motion along the x- and y-axes, implemented via hexagonal coil arrangements. The conceptual foundation of this motor was initially proposed in. Subsequent analyses of Lorentz forces acting on individual conductor segments enabled the realization of decoupled control for each degree of freedom through independent current inputs [14–15]. However, similar to other SBM designs, prior studies have primarily demonstrated the feasibility of decoupling without quantifying the proportionality coefficients between generated forces/torque and their corresponding currents.

This paper addresses this limitation by conducting a series of experimental measurements to determine the force and torque outputs, thereby validating the theoretical model. The principal contribution of this study lies in the development of a dedicated measurement system for force and torque, enabling comprehensive evaluation of motor performance and providing empirical support for theoretical predictions.

The remainder of this paper is structured as follows: Section 2 details the motor configuration, operating principles, and control architecture; Section 3 outlines the experimental setup and data acquisition methodology; Section 4 presents and discusses the experimental results; and Section 5 concludes the paper and proposes directions for future research.

2. Structure, working principle, and control

2.1 Motor structure and working principle

The motor structure was introduced in study [14] and is detaily described in Figure 1. It is shown that 2 main parts of the motor are rotor and stator. The rotor consists of an radial magnetized permanent magnet which utilizes an external iron casing to fabricate a closed magnetic circuit. These two parts of the rotor are attached by an aluminum clamping fixture. And the stator is positioned in the air gap region.
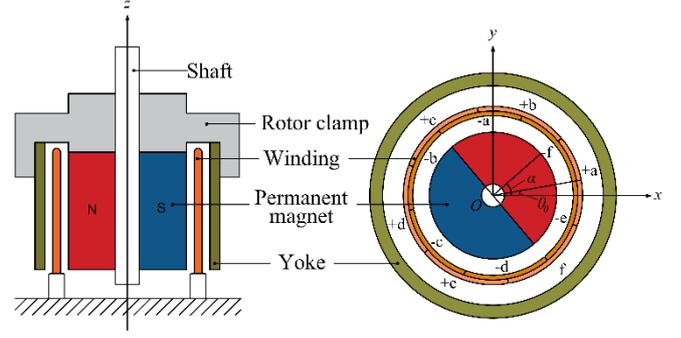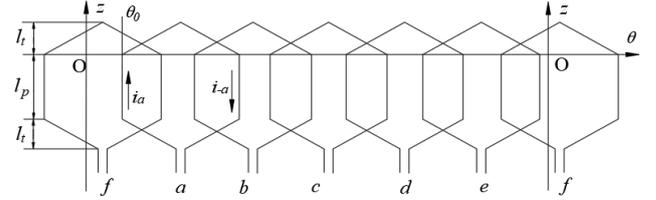

Figure 1: Slotless self-bearing motor structure

Figure 2: Winding configuration in z-θ plane

The motor stator comprises six phases which are labeled a, b, c, d, e and f respectively, they are symmetrically arranged on the circular path inside the rotor air gap. The stator windings are mechanically fixed using non-magnetic materials. Each stator phase contains n windings, each one is wound into a hexagonal form. When the stator was mounted on the motor, an angle of $\pi/2$ radians of the stator is covered by each phase. Additionally, the angular distance between 2 adjacent phases is $\pi/3$. Each winding consists of two main parts: a parallel component l_p and a serial component l_t. Two parallel segmets l_p in a same winding are arranged with an angular displacement of $\pi/4$. The illustrated diagram in Figure 2 shows the winding distribution where each phase winding is reduced to a single coil for simplicity.

By applying currents to the stator phases, the motor produces bearing forces F_x, F_y c along the x- and y-axis, while simultaneously generating rotational torque τ. Following the Lorentz force principle and a force-synthesis approach, study [14] demonstrated the motor potential to generate rotational torque and bearing forces along mutually independent radial directions, each driven by a separate current. For clarity in derivation, the theoretical analysis assumes operation within the linear magnetic region; furthermore, the slotless stator design allows us to neglect high-order harmonic effects in this fundamental validation. Under these assumptions, the equations describing force and torque generation in the SSBM are expressed as follows:

$$\begin{cases} \tau = k_{nm} \, k_m \, i_m \\ F_x = -k_{nb} \, k_b \, i_x \\ F_y = -k_{nb} \, k_b \, i_y \end{cases} \tag{1}$$

with τ is designated as the motor rotation torque; F_x, F_y are respectively the motor radial bearing forces corresponding to x- and y-axis directions; i_m, i_x, i_y are currents generating the above torque and forces. The remaining coefficients are described as the following equations:

$$k_{nm} = 1 + 2\cos\left(\frac{\pi}{3n}\right) + 2\cos\left(2\frac{\pi}{3n}\right) + \cdots$$
$$+ 2\cos\left(\frac{n-1}{2}\frac{\pi}{3n}\right)$$

$$k_m = \left(3\sqrt{2}l_p + \frac{8(6-3\sqrt{2})}{\pi}l_t\right)rB_0 \qquad (2)$$

$$k_{nb} = 1 + 2\cos\left(2\frac{\pi}{3n}\right) + 2\cos\left(4\frac{\pi}{3n}\right) + \cdots$$
$$+ 2\cos\left((n-1)\frac{\pi}{3n}\right)$$

$$k_b = \left(3l_p + \frac{12}{\pi}l_t\right)B_0$$

Herein, r is rotor radius; B_0 is the maximum value of the magnetic flux density applied to the coil. Moreover, the currents placed in stator phases are the superposition of the mentioned individual curents, are described in [14] by the formulation (3):

$$\begin{cases} i_{a,d} = i_x \sin(\alpha) + i_y \cos(\alpha) \pm i_m \cos(\beta) \\ i_{b,e} = i_x \sin(\alpha - 2\pi/3) + i_y \cos(\alpha - 2\pi/3) \\ \qquad \pm i_m \cos(\beta + \pi/3) \\ i_{c,f} = i_x \sin(\alpha - 4\pi/3) + i_y \cos(\alpha - 4\pi/3) \\ \qquad \pm i_m \cos(\beta + 2\pi/3) \end{cases} \qquad (3)$$

In this equation, α is the angular postion of the rotor while β is the angle of the torque generated current with $\beta = \alpha - \pi/4$.

On the basis of the mentioned configuration and working principle, a control structure is specifically constructed for confirmation the theoretical results by comparing them with the experimental outcomes.

2.2 Control structure

In this study, Oxy coordinate system is applied as in discription in Figure 1. It is assumed that the forces acting on the motor are uniformly distributed and concentrated at the center of mass. Concurrently, under small displacement conditions, the rotor motion along the Ox and Oy directions is considered as linear translation. Consequently, the rotor dynamic equations are derived as follows:

$$\begin{cases} \ddot{x} = F_x/m \\ \ddot{y} = F_y/m \\ \dot{\omega} = \tau/J \end{cases} \qquad (4)$$

Herein, x and y are the coordinates of the rotor in Oxy coordinate system; m is the mass; ω is the rotation velocity; and J is the rotor moment of inertia.

In equation (4), each dynamic equation of the motor is respectively corresponded to a independent control current in equation (1). Therefore, individual control loops can be designed for each kinematic variable, including the rotor positions along the x- and y-axis, and motor speed ω. For the rotor position along the x- and y-axis, the transfer function is a second-order integrator, and therefore a PID controller is required for stabilization. The transfer function of the PID controller is as follows:

$$k_P\left(1 + \frac{1}{T_I s} + T_D s\right) \qquad (5)$$

With the aim of the stability in the system, the PID controller coefficients are determined in [14] by the formulation:

$$k_P = \frac{3s_0^2}{K_f}, T_I = \frac{3}{s_0}, T_D = \frac{1}{s_0} \qquad (6)$$

With $K_f = k_{nb}k_b/m$, and s_0 has to be evaluated in order that $s_0 > 0, s_0 \in R$. On the other hand, for the motor speed ω, a PI controller has been used since the transfer function is only a first-order integrator. The transfer function of the PI controller is as follows:

$$k_{P\omega}\left(1 + \frac{1}{T_{I\omega}s}\right) \qquad (7)$$

Similar to PID controller, the PI controller coefficients are also established to ensure system stability as follows:

$$k_{P\omega} = \frac{2s_{0\omega}}{K_{T\omega}}, T_{I\omega} = \frac{2}{s_{0\omega}} \qquad (8)$$

With $K_{T\omega} = k_{nm}k_m/J$, and $s_{0\omega}$ is identified so that $s_{0\omega} > 0, s_{0\omega} \in R$. The evaluations of s_0 and $s_{0\omega}$ can affect directly to the stability of the system. To balance system performance and the capacity of the power circuit, the values of s_0 and $s_{0\omega}$ must be carefully chosen.

Figure 3 presents the motor control structure. In this model, the control variables x-axis, y-axis positions and motor speed ω are manipulated by individually control loops. Sensor feedbacks for the positions and speed are utilized as response signals for the controllers. The axis positions are determined by PID controllers, while a PI controller is used to regulate the motor speed. Using Park-Clark transformations, the current values calculated by the controllers are transformed into currents distributed across the six phases of the motor stator. The signals corresponding to these currents are transmitted to the motor driver, which subsequently actuates the motor. This control configuration allows the control of the motor speed and maintains motor positions stability along x- and y- axis.

3. Experimental setup

The experimental model is configured specifically to measure and examine the key parameters of the prototype motor, that includes bearing force, rotational torque, rotation speed and phase current. Then the result is revealed to validate the accuracy of the theoretical formulas developed earlier.

The motor prototype was designed and subjected to investigation with the parameters listed in Table 1. The control algorithm was developed in MATLAB/Simulink on the host computer and subsequently deployed to the dSPACE MicroAutoBox III via Ethernet for real-time execution. Additionally, the dSPACE ControlDesk application was employed to monitor and control the motor's performance and status. This software enables the activation and deactivation of control functions, parameter adjustment, and real-time data recording of sensor values and control signals.
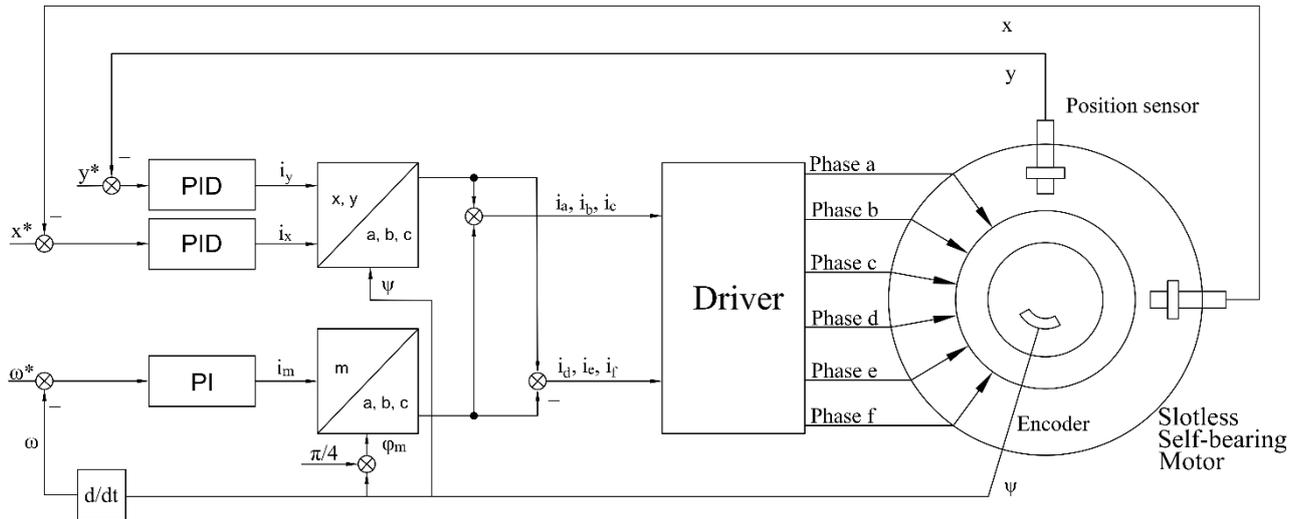
Figure 3: Control structure of slotless self-bearing motor

Table 1: Parameters of experimental motor

Parameters	Symbol	Value
Rotor mass	m	0.4 kg
Rotor magnetic outer radius	r_m	0.02 m
Rotor yoke inner radius	r	0.025 m
Stator outer radius	R	0.022 m
Maximum magnetic flux density in the air gap	B_0	0.59 T
Number of turns per coil	n	55
Winding diameter	d	0.0008 m
Length of parallel conductor part	l_p	0.008 m
Length of serial conductor part	l_t	0.006 m
Moment of inertia	J	9.68×10^{-5} kg.m^2

The rotor rotational angle was measured using a incremental encoder integrated into the Sigma-5 SGMJV servo motor, which is mounted on the same shaft as the SSBM. Instead of a rigid connection, the servo motor is coupled to the SSBM rotor via a universal joint. This configuration fixes the z-axis for 3-DOF control. Furthermore, due to the high ratio of shaft length to air gap size, the rotor's angular motion is approximated as linear radial displacement (x, y). The rotor position was measured using two VS-202-M proximity sensors based on the eddy current principle, with rotor displacement considered within a range of 0-2 mm. These signals were acquired and processed through the ADC input channels of the MicroAutoBox III.

The motor driver is a power amplifier used to control the stator phase currents. It has six input terminals for receiving controller voltages and six output terminals corresponding to the six stator phases. At first, the phase current reference signals, which were expressed as voltage signals at a ratio of 1 V per 1 A of the desired phase current, were calculated and generated by the controller. These voltage signals were then transmitted to the power amplifier inputs via the six DAC output channels of the MicroAutoBox III. Finally, the power amplifier supplied the actual currents to each phase of the stator windings.
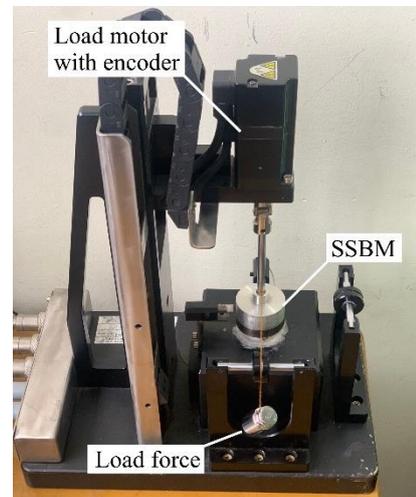

Figure 4: Expemirental motor structure

For force measurement experiment, an indirect approach based on the force equilibrium was applied. To analyzed the generated bearing force, a weight of mass m was attached to the motor shaft along x-axis and y-axis directions. In the meantime, the rotor bearing force acting along x or y direction occupied a magnitude which is equal to that of the weight gravitational force $F_g = m\,g$. The control system was established in order to stabilize the motor at its equilibrium position. In this state, the bearing force generated by phase currents will be exactly equal to the weight gravitational force. From this, the relationship between the bearing force and the current producing it can be detemined. In addition, for the torque measurement experiment, the prototype motor is mounted on a same shaft with a load motor that is capable of setting a desired torque value. During the control process, the torque-generating current i_m, at a constant rotational speed ω, is compared under friction load only and under gradually increased torque load, as a result, the experiment obtained the current producing the torque value imposed by the torque load motor. The experimental motor configuration is presented in Figure 4 while the overall experimental setup is shown in Figure 5.
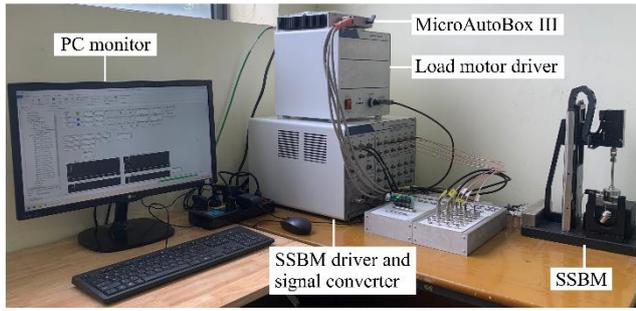
Figure 5: Experimental system

In the next section, the experimental outcomes will be illustrated for a detailed review and comparison with the theoretical equations.
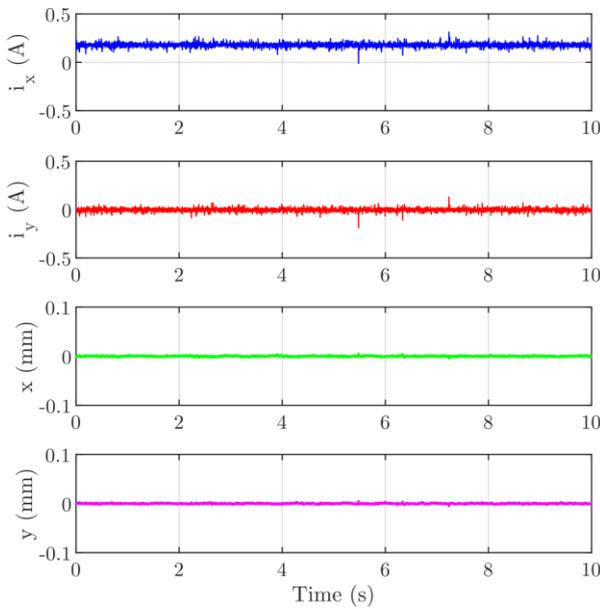
4. Experimental results

Figure 6: Measured currents i_x, i_y and positions x, y under a 0.2 N force applied along the x-axis

To comprehensively validate the theoretical model and evaluate the key operating characteristics of the SSBM, the experimental study is conducted in three distinct phases. Initially, the study focuses on the static force and torque characteristics to verify the fundamental linearity of the forces/torque and the corresponding current while the motor is stationary. Subsequently, the impact of the rotor phase angle α on force generation is analized, ensures that the radial forces remain decoupled from rotor position. The final phase investigates the dynamic behavior of the motor, specifically evaluating how variations in rotational speed influence the force-current relationship and identifying any high-speed coupling effects.

In the static validation phase, the experiment verified the correlation between the bearing forces and their generating currents. It is shown that when there is an external force applied in traverse direction, the control current will regulate to maintain the motor at its equilibrium position. In Figure 6, with a 0.02 kg weight suspended to the motor along the x-axis, the currents results were derived while the motor was kept stationary. Taking that into consideration, when there was a

traverse force along x-axis, only the current value i_x varied to ensure that the motor was held stationary, while i_y slightly oscillated around zero.

It can be observed in Figure 7 that the experimental results (noted as Exp.) closely follow the theoretical line (noted as Theory) derived from previous studies. The average relative error between the measured current and the theoretical prediction was approximately 0.87% for the x-axis bearing force. This low discrepancy validates the linearity of the relationship between the current i_x and the generated force F_x, More specifically, confirming the accuracy of the coefficient in the equation $F_x = k_{nb}k_b i_x$.
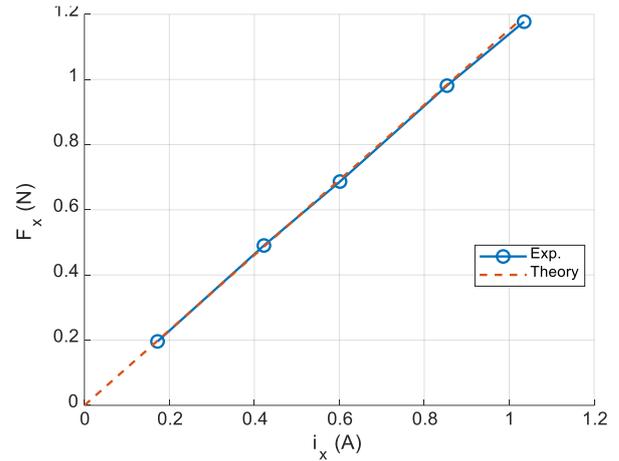

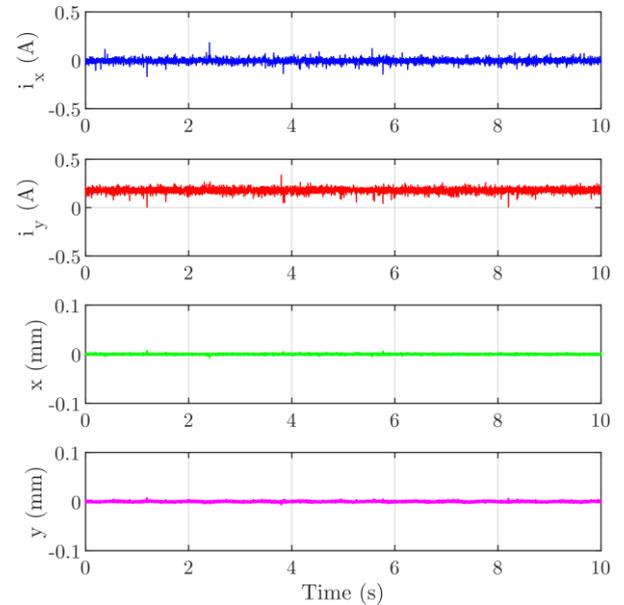**Figure 7:** Relationship between current i_x and force F_x along the x-axis

Figure 8: Measured currents i_x, i_y and positions x, y under a 0.2 N force applied along the y-axis

Similar to the test along x-axis, the motor was kept stationary while being attached a 0.02 kg weight along y-axis, the measured current values i_x, i_y and the motor position along x- and y-axis were also recorded and can be observed in Figure 8. From the figure, it is clear that without influencing the motor x-axis motion, the independent control along y-axis yet, still be able to obtaine. By continuously varying the force value employed on the motor along y-axis, the result presented in Figure 9 exhibit a consistent linear trend as in

Figure 7. The quantitative evaluation indicates an average relative error of 3.51% between the experiment and theoretical prediction. This confirms that the independent control of the y-axis force is achieved with high precision.
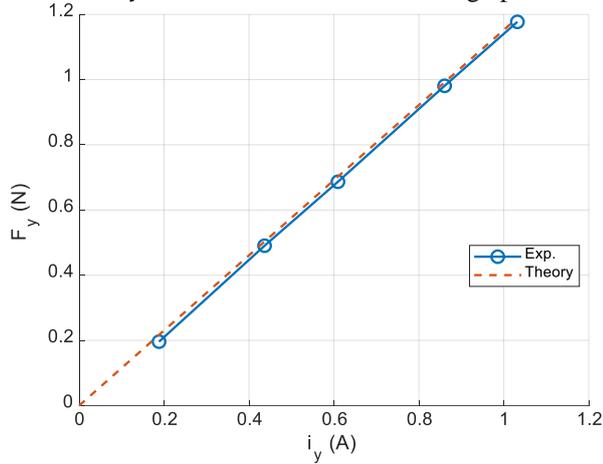

Figure 9: Relationship between current i_y and force F_y along the y-axis
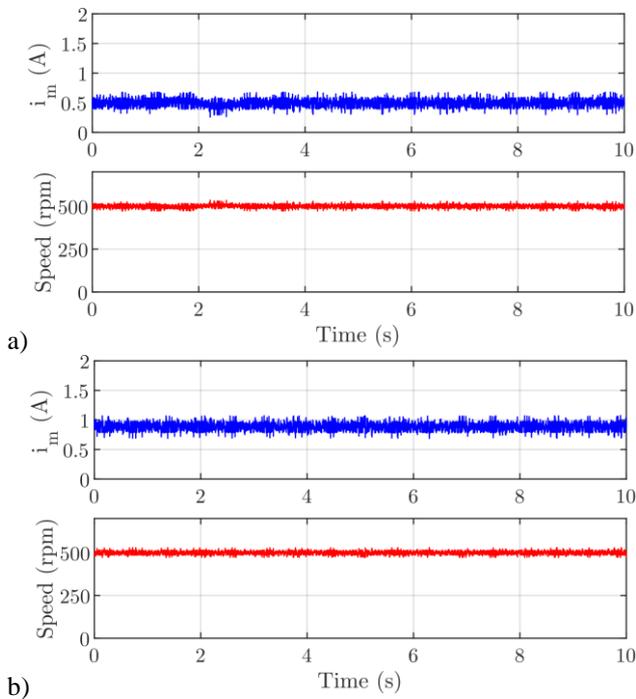

a)

b)

Figure 10: Torque current i_m at 500 rpm with (a) only frictional load and (b) additional torque load of 0.015 N·m

For validating the relationship between the generated motor torque and its corresponding current, the experiment applied a set value of torque load to the motor, simutaneously controlled the motor to rotate at a stable velocity and the current value i_m, after neglect the friction load, represented the current needed to produce a torque that balanced the employed load.

The obtained results shown in Figure 10 illustrate that when the same velocity is applied, the difference between two current values i_m in two corresponding cases, with and without a torque load of 0.015 N·m. This difference is the explicit amount of current required to produce a torque with the magnitude of 0.015 N·m. By applying different torque load values, the correlation betweern the generated torque τ

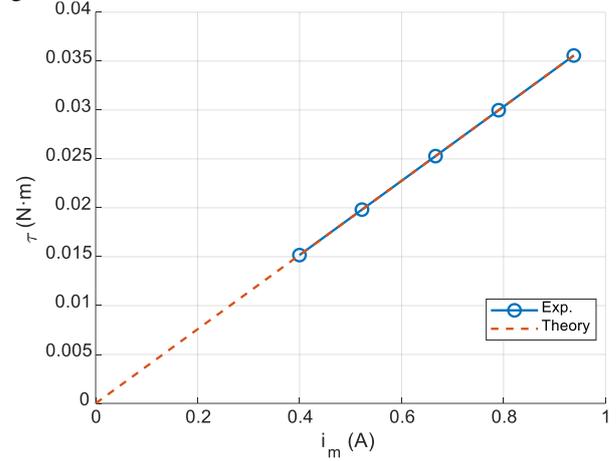and the current producing it i_m was achieved and presented in Figure 11.

Figure 11: Relationship between current i_m and rotational torque τ

Similarly with the results of i-F shown in Figure 7 and Figure 9, the experimental data demonstrates a highly linear characteristic. The measured torque constant deviates from the theoretical value $k_{nm} k_m$ by an average margin of only 0.97%. This result provides empirical verification of the theoretical torque-current relationship established in the motor model.
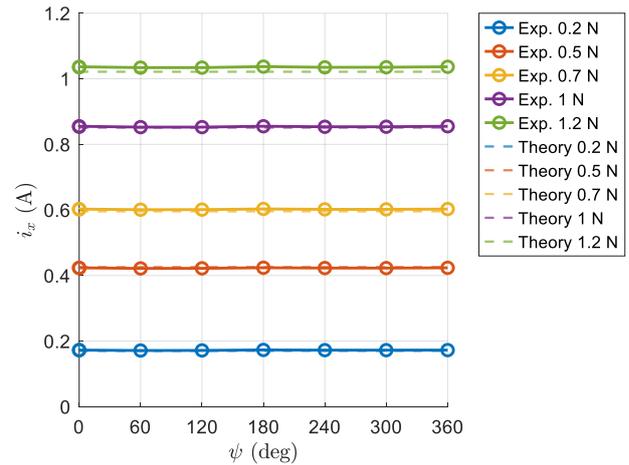

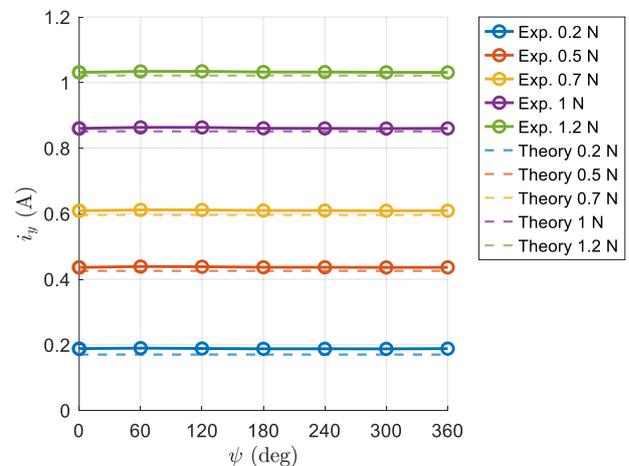**Figure 12:** Current i_x with rotor angle ψ under various force loads along the x-axis

Figure 13: Current i_y with rotor angle ψ under various force loads along the y-axis

Next, the influence of the rotor rotational angle α on the radial bearing forces was examined. In this experiment, the rotor phase angle was constantly held at $0, \pi/3, 2\pi/3, \pi, 4\pi/3$ and $5\pi/3$ rad while the motor control current was measured at different applied force values along the same x- or y-axis direction. The experiment result in Figure 12 show that when a constant force magnitude is applied, the required control current i_x remains stable across different phase angles. This outcome remains accurate even as applying different values of the force F_x along x-axis. The data indicates a maximum variation of less than 0.54% relative to the mean current value across all tested angles. A similar stability is observed for the y-axis control current i_y in Figure 13, with a maximum fluctuation of 0.68%. These negligible variations confirm that the direction and magnitude of the forces generated by i_x and i_y are effectively decoupled from the rotor rotational angle α, validating the theoretical assumption of isotropic force generation.
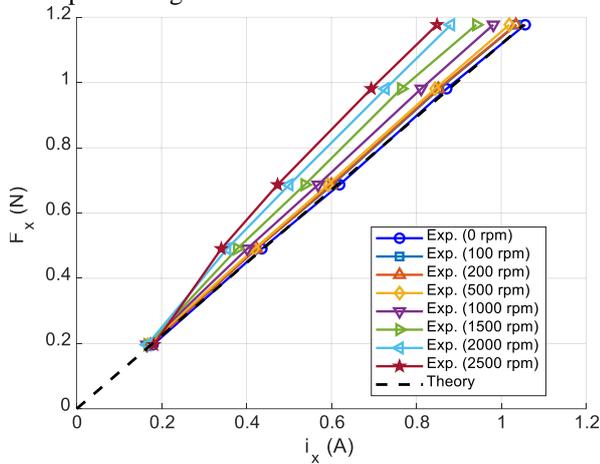

Figure 14: Influence of speed on the current-force relationship along the x-axis
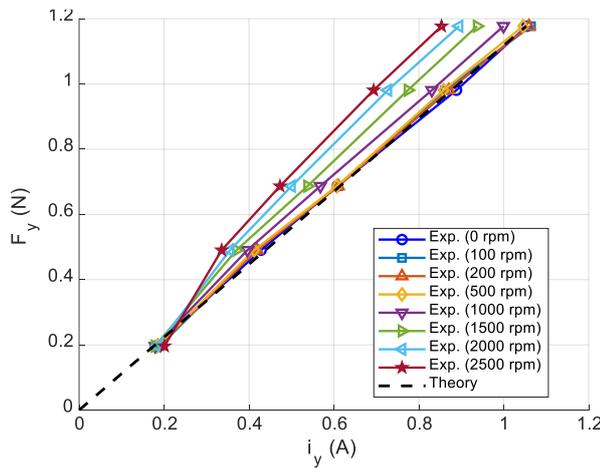

Figure 15: Influence of speed on the current-force relationship along the y-axis

Finally, regarding the dynamic speed influence, the correlation between the produced force and its corresponding current was validated while applying stable speeds to the motor. The obtained results, corresponding to along x-axis and along y-axis instances, are shown in Figure 14 and 15. The experiment characteristics were observe at the employed speeds of $100, 200, 500, 1000, 1500, 2000, 2500$ rpm,

respectively. At the speed range below 500 rpm, the experimental i-F plot was relatively consistent and closely follows that of the theoretical. Howerver, as the speed increased, this i-F line started to gradually deviate from the initial theoretical result. With a small force load, changing speed barely made any significant impacts on the control current value, yet, as the load value and speed increased, for the same required generated force, the utilized current needed decreared. At the speed of 1000 rpm along x-axis, the i-F line substantially diverges as the load increases and at the time the load reaches 1.2 N, the divergence becomes 4% deviated from the theory. Identical outcomes happen at higher speeds. The attained errors are 7.9, 13.7, 16.9% corresponding to the speeds at 1500, 2000 and 2500 rpm. In addition, along y-axis, the obtained errors in the 1000-2500 rpm speed range are 2.2, 8.3, 12.4 and 16.4%. These results demonstrate that coupling effects between the current control loop and postion control loops have taken place. In order to overcome this difficulty, the mutual interaction influence of the motor speed and bearing forces, as well as an advanced control system developing a speed–position decoupling algorithm, need to be taken into consideration for further research.

5. Conclusion

This study presented a comprehensive characteristic analysis of a SSBM, specifically examining the generation of radial forces F_x, F_y and rotational torque τ. The experimental validation confirmed that the bearing force and torque outputs of the motor exhibit a high degree of linearity with respect to the corresponding currents, closely aligning with the theoretical Lorentz force model across the tested load range. Furthermore, the study verified that the magnitude and direction of the generated radial forces were found to be independent of the rotor phase angle α, demonstrating that the proposed winding configuration effectively decouples the suspension control from the rotor position.

However, experiments reveal a clear speed dependence: at elevated rotational speeds, measured forces deviate significantly from the theoretical predictions, suggesting uncompensated coupling between torque and suspension control loops. Future work will therefore develop a comprehensive mathematical model for the observed speed-dependent nonlinearities and implement advanced decoupling/adaptive control strategies to ensure stable operation across the entire speed range.

Acknowledgement

References

[1] Sun, X., Chen, L., & Yang, Z. (2012). Overview of Bearingless Permanent-Magnet Synchronous Motors. *IEEE Transactions on Industrial Electronics*, *60*(12), 5528–5538.

[2] Liu, B. (2015). Survey of bearingless motor technologies and applications. *2022 IEEE International Conference on Mechatronics and Automation (ICMA)*, *9*, 1983–1988.

[3]   Chen, J., Zhu, J., & Severson, E. L. (2019). Review of Bearingless mo-
      tor Technology for significant power Applications. *IEEE Transactions
      on Industry Applications*, *56*(2), 1377–1388.

[4]   Casemore, M., & Stephens, L. (1999). Actuator gains for a toothless
      permanent-magnet self-bearing motor. IEEE Transactions on Magnet-
      ics, 35(6), 4482–4489.

[5]   Stephens, L. S., & Kim, D. (2000). Analysis and simulation of a Lo-
      rentz-Type slotless, Self-Bearing motor. IFAC Proceedings Volumes,
      33(26), 449–454.

[6]   Ren, N. Z., & Stephens, L. (2006). Force characteristics and gain deter-
      mination for a slotless self-bearing motor. *IEEE Transactions on Mag-
      netics*, *42*(7), 1849–1860.

[7]   Ren, N. Z., Stephens, L., & Radun, A. (2006). Improvements on wind-
      ing flux models for a slotless self-bearing motor. *IEEE Transactions on
      Magnetics*, *42*(7), 1838–1848.

[8]   Ueno, S., Uematsu, S., & Kato, T. (2009). Development of a Lorentz-
      Force-Type slotless Self-Bearing motor. *Journal of System Design and
      Dynamics*, *3*(4), 462–470.

[9]   Steinert, D., Nussbaumer, T., & Kolar, J. W. (2013, May). Concept of a
      150 krpm bearingless slotless disc drive with combined windings (Paper
      No. IEMDC. 2013.6556269). In 2013 IEEE International Electric Ma-
      chines & Drives Conference (IEMDC). IEEE.

[10] Baumgartner, T., Burkart, R. M., & Kolar, J. W. (2013). Analysis and
      Design of a 300-W 500 000-r/min Slotless Self-Bearing Permanent-
      Magnet Motor. *IEEE Transactions on Industrial Electronics*, *61*(8),
      4326–4336.

[11] Gallego, G. B., Rossini, L., Achtnich, T., Araujo, D. M., & Perriard,
      Y. (2021). Efficiency optimization of slotless Magnetic-Bearing ma-
      chines. *IEEE Transactions on Industry Applications*, *57*(6), 6833–
      6843.

[12] Nguyen, Q., Nguyen, H., Nguyen, K., Vo, D., Nguyen, X., Ueno, S.,
      & Giap, V. (2022). Correction: Robust sliding mode control for
      Slotless-Self bearing motor system. *Journal of Electrical Engineering
      and Technology*.

[13] N Nguyen, Q. D., Nguyen, H. P., Vo, D. N., Nguyen, X. B., Ueno, S.,
      Huang, S., & Giap, V. N. (2022). Robust sliding mode Control-Based
      a novel Super-Twisting disturbance observer and Fixed-Time state
      Observer for Slotless-Self bearing motor system. *IEEE Access*, *10*,
      23980–23994.

[1]   Nguyen, H. P., Nguyen, X. B., Bui, T. T., Ueno, S., & Nguyen, Q. D.
      (2019). Analysis and control of slotless Self-Bearing
      Motor. *Actuators*, *8*(3), 57.